A Pyridinic Fe-N_4 Macrocycle Effectively Models the Active Sites in Fe/N-Doped Carbon Electrocatalysts

Travis Marshall-Roth,[1] Nicole J. Libretto,[2,3] Alexandra T. Wrobel,[4] Kevin J. Anderton,[4] Nathan, D. Ricke,[1] Troy Van Voorhis,[1] Jeffrey T. Miller,[2,3] and Yogesh Surendranath[1,*]

[1] Department of Chemistry, Massachusetts Institute of Technology, Cambridge, Massachusetts 02139, United States

[2] Davidson School of Chemical Engineering, Purdue University, West Lafayette, Indiana 47097, United States

[3] Chemical Science and Engineering Division, Argonne National Laboratory, Argonne, Illinois 60439, United States

[4] Department of Chemistry and Chemical Biology, Harvard University, Cambridge Massachusetts 02138, United States

ABSTRACT

Iron- and nitrogen-doped carbon (Fe-N-C) materials are leading candidates to replace platinum in fuel cells, but their active site structures are poorly understood. A leading postulate is that iron active sites in this class of materials exist in an Fe-N_4 pyridinic ligation environment. Yet, molecular Fe-based catalysts for the oxygen reduction reaction (ORR) generally feature pyrrolic coordination and pyridinic Fe-N_4 catalysts are, to the best of our knowledge, non-existent. We report the synthesis and characterization of a molecular pyridinic hexaazacyclophane macrocycle, ($phen_2N_2$)Fe, and compare its spectroscopic, electrochemical, and catalytic properties for oxygen reduction to a prototypical Fe-N-C material and iron octaethylporphyrin, (OEP)Fe, a prototypical pyrrolic iron macrocycle. N 1s XPS signatures for coordinated N atoms in ($phen_2N_2$)Fe are positively shifted relative to (OEP)Fe, and overlay with those of Fe-N-C. Likewise, spectroscopic XAS signatures of ($phen_2N_2$)Fe are distinct from those of (OEP)Fe, and are remarkably similar to those of Fe-N-C with compressed Fe–N bond lengths of 1.97 Å in ($phen_2N_2$)Fe that are similar to the average 1.94 Å length in Fe-N-C. Electrochemical data indicate that the iron center in ($phen_2N_2$)Fe is relatively electropositive, with an Fe(III)-OH/Fe(II)-OH_2 potential at 0.59 V vs the reversible hydrogen electrode (RHE), ~300 mV positive of (OEP)Fe. This correlates with a 300 mV positive shift in the onset of ORR catalysis for ($phen_2N_2$)Fe with a corresponding 1400-fold increase in TOF relative to (OEP)Fe. Consequently, the ORR onset for ($phen_2N_2$)Fe is within 150 mV of Fe-N-C. Unlike (OEP)Fe, ($phen_2N_2$)Fe displays excellent selectivity for 4-electron ORR with <4% maximum H_2O_2 production, comparable to Fe-N-C materials. This study establishes a pyridinic iron macrocycle that effectively models Fe-N-C active sites and provides a rich platform for constructing high-performance Fe-based oxygen reduction catalysts.

MAIN

The four-electron, four-proton reduction of molecular oxygen to water is the efficiency-limiting half reaction in low temperature fuel cells.[1,2] Regardless of the fuel source used, the current density output is primarily limited by the slow electron transfer kinetics of the oxygen reduction reaction (ORR) taking place at the cathode.[3] The sluggish kinetics involved in this half reaction necessitate high catalyst loadings at the cathode to generate practical current densities. The prototypical material for catalyzing this reaction in commercial fuel cells is platinum metal (Pt) supported on carbon. However, the high cost and scarcity of Pt impedes the large-scale deployment of fuel cell devices and motivates the development of Earth-abundant electrocatalysts for oxygen reduction. These catalysts must operate at low overpotentials[4–6] and with high selectivity for the four-electron reduction of oxygen to water over the two-electron reduction process to generate hydrogen peroxide.[7–10] Since early reports of oxygen reduction catalyzed by macrocyclic first-row transition metal complexes,[11,12] there has been a global effort to develop selective and efficient ORR catalysts featuring base metal active sites.[13]

Pyrolyzed iron- and nitrogen-doped (Fe-N-C) materials are leading Earth-abundant alternatives to Pt-based ORR electrocatalysts,[14] however significant increases in catalyst performance are needed to make these materials technologically viable. Systematic improvement of these materials is hampered by the limited molecular-level understanding or control of the iron active sites.[15] Fe-N-C materials are typically prepared by the high temperature pyrolysis of finely dispersed iron salts[16], porphyrins,[17,18] or phthalocyanines[19] along with a metal-organic framework (MOF)[20,21] or carbon-based support.[22–25] The uncontrolled nature of pyrolysis leads to a wide diversity of iron environments as well as extended solid iron phases in the resulting Fe-N-C materials.[26,27] This poor control, combined with the wide variability in preparative procedures, has led to longstanding uncertainty about the local structure of the iron active sites responsible for ORR, thereby impeding systematic improvements to catalytic performance.[28]

Numerous recent studies have provided significant insight into possible active site structures on Fe-N-C materials. While metallic iron has been postulated as an active site,[29,30] mononuclear Fe-N_4 active sites are more commonly invoked to explain correlations between X-ray absorption spectroscopy (XAS) or ^{57}Fe Mössbauer spectroscopy with ORR activity.[16,24,31–38] Despite the growing consensus that Fe-N_4 sites are essential for ORR, the ligation environment of these iron sites remains uncertain.[34,39] Indeed, even though iron porphyrin and phthalocyanine complexes can be used as precursors to Fe-N-C materials, there is growing appreciation that the core pyrrolic ligation environment of these precursors changes substantially upon pyrolysis.[40–43] In particular, the first shell Fe–N bond lengths in Fe-N-C materials have been reported to be substantially shorter than the macrocyclic iron complex precursor used in the material synthesis.[17] Furthermore, X-ray photoelectron spectroscopy (XPS) studies have pointed to the presence of metal-coordinated pyridinic nitrogen moieties as opposed to metal-bound pyrrolic nitrogens in Fe-N-C materials.[44–48] ^{57}Fe Mössbauer spectra of many iron porphyrin[49–53] and phthalocyanine[54–59] complexes differ dramatically from main ^{57}Fe Mössbauer doublets assigned to the putative Fe-N_4 actives sites in Fe-N-C materials.[60–62] In addition, atomic-resolution TEM data indicates the presence of mono-dispersed iron atoms bound in within the plane of graphitic carbon[63–67] suggesting that the ligating groups are 6-membered heterocycles rather than the 5-membered rings found in porphyrins and phthalocyanines. Based on these spectroscopic and imaging results, there is a growing body of evidence that the Fe-N_4 sites in Fe-N-C materials are ligated by pyridinic moieties fused within graphitic sheets (Scheme 1a).

Despite substantial evidence for *pyridinic* Fe-N_4 sites in Fe-N-C materials, nearly all molecular Fe-based ORR catalysts are macrocyclic complexes that feature *pyrrolic* coordination environments (Scheme 1b). Studies on homogeneous and adsorbed pyrrolic Fe complexes have shed significant insight into the mechanistic aspects of ORR including structure-function correlations and scaling relationships.[68–75] However, the pyrrolic coordination environment of these molecular complexes makes them ineffective models for Fe-N-C materials, complicating spectroscopic assignments, and structure-activity correlations. Indeed, adsorbed pyrrolic Fe macrocycles generally display inferior activity and selectivity for ORR relative to Fe-N-C materials.[17] Clearly, systematic progress in the understanding of Fe-N-C active sites and the rational design of improved catalysts requires new Fe-N_4 molecular complexes that can serve as high fidelity structural and functional mimics of Fe-N-C materials.

Based on the aggregate spectroscopic evidence on Fe-N-C materials, we envisioned that a high fidelity model would feature: (a) a tetrapyridinic coordination environment, (b) relatively short Fe–N bond lengths,[17] (c) an extended ligand π system[41,42] capable of stabilizing the Fe(II) state[76,77] and (d) a relatively high Fe(III)-OH/Fe(II)-OH_2 redox potential. We envisioned that a model complex fulfilling each of these criteria would provide a firm basis for drawing molecular-level insight into the behavior of Fe-N-C materials while simultaneously providing a new platform for the bottom up design of high-performance molecular ORR catalysts.

Towards realizing the above goal, we searched the literature for pyridinic N_4 macrocyclic ligands. Notably, the aza-bridged bis-1,10-phenanthroline hexaazamacrocycle, ($phen_2N_2$)H_2 ($phen_2N_2$ = 1,14:7,8-diethenotetrapyrido[2,1,6-*de*:2',1',6'-*gh*:2",1",6"-*kl*:2"',1"',6"'-*na*][1,3,5,8,10,12]hexaazacyclotetradecine), as well as its cobalt(II), nickel(II) and copper(II) complexes have been reported[78–83] and applied to DNA binding studies[84] and carbon dioxide reduction catalysis.[85–88] Despite this precedent, the synthesis and ORR activity of the corresponding ($phen_2N_2$)Fe fragment[77] has, to the best of our knowledge, been unexplored. Herein, we report the synthesis and characterization of this pyridinic Fe-N_4 macrocyclic fragment (Scheme 1c) and compare its ^{57}Fe Mössbauer, XPS, and XAS features and ORR performance to those of prototypical Fe-N-C and octaethylporphyrin (OEP)Fe catalysts. Through these studies, we demonstrate that the iron coordination environment in [($phen_2N_2$)Fe]$_2$O closely resembles that of Fe-N-C materials and that ($phen_2N_2$)FeCl displays superior catalytic activity and selectivity relative to (OEP)FeCl, closely approaching the performance metrics of Fe-N-C materials. These studies establish ($phen_2N_2$)Fe complexes as high-fidelity structural and functional mimics of Fe-N_4 active sites in Fe-N-C materials.

Scheme 1. Putative pyridinic Fe-N_4 active site in Fe-N-C materials (a). Molecular structures of (OEP)Fe (b) and ($phen_2N_2$)Fe (c) model compounds.

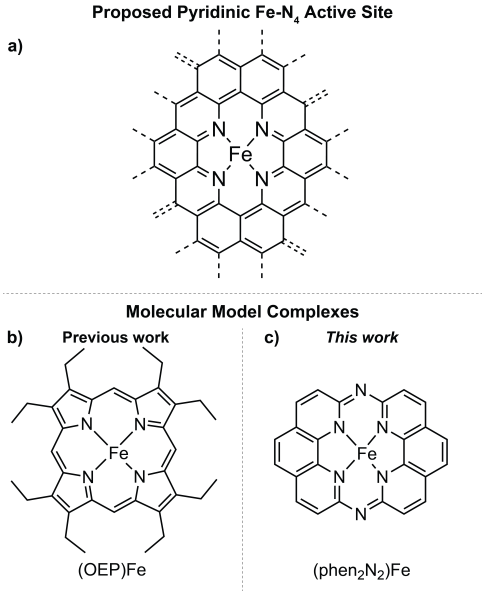

RESULTS AND DISCUSSION

Synthesis and Initial Characterization of Fe-N-C, Fe-porphyrin and ($phen_2N_2$)Fe Complexes. A prototypical Fe-N-C material was synthesized by a combination of literature methods.[20,89] Briefly, Fe-N-C was prepared by pyrolysis of a mixture of iron(II) acetate, 1,10-phenanthroline and ZIF-8 metal organic framework under a reducing atmosphere (5% H_2 in Ar). After pyrolysis, the sample was washed with 0.1 M H_2SO_4 to remove trace Fe(0). The ^{57}Fe Mössbauer spectrum of this material (Figure 1, top) displays two quadrupole doublets. The narrow doublet, commonly referred to as the D1 doublet,[90] displays an isomer shift (δ) of 0.46 mm s^{-1} and a quadrupole splitting ($|\Delta E_Q|$) of 1.08 mm s^{-1} and the wide doublet, commonly referred to as the D2 doublet,[90] is characterized by δ = 0.37 mm s^{-1} and $|\Delta E_Q|$ = 3.06 mm s^{-1}. These parameters are in line with previously reported Fe-N-C materials (see Table S1 for a comparison of ^{57}Fe Mössbauer parameters). These features were recently postulated to arise from Fe-N_4 sites existing in high-spin Fe(III) and low-spin Fe(II) states, respectively,[90] although other assignments have been made previously, including D1 as a low spin Fe(II) site and D2 as an intermediate spin Fe(II) site.[16,17,60]

The bis-phenanthroline macrocycle, ($phen_2N_2$)H_2, was prepared by a modified literature procedure.[80] In brief, the macrocyclization was achieved by exposure of 2,9-dichlorophenanthroline to anhydrous ammonia in a Parr reactor held at 280 °C for 24 hours and then ramped to 300 °C for 12 hours (Scheme 2). Metalation with iron was achieved by treating ($phen_2N_2$)H_2 with anhydrous $FeCl_3$ in DMF or HMPA in the presence of excess tributylamine under an N_2

Scheme 2. Synthetic route to ($phen_2N_2$)H_2, ($phen_2N_2$)FeCl and [($phen_2N_2$)Fe]$_2$O from 2,9-dichloro-1,10-phenanthroline.

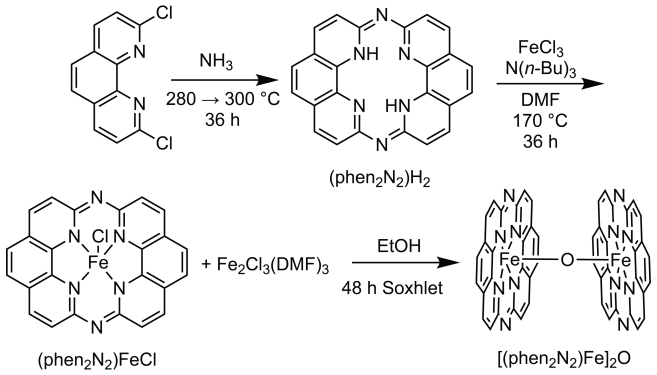

atmosphere. To remove unreacted $FeCl_3$ and other reaction byproducts, the crude reaction mixture was then washed with copious amounts of diethyl ether and dichloromethane. Due to the extremely low solubility of the $(phen_2N_2)FeCl$ complex, we found that residual Fe_2Cl_6•$(DMF)_3$ (~16%) remained in the sample despite exhaustive washing with anhydrous solvents (see SI for details).[91] HR-MS analysis of the material reveals a prominent peak at 440.1061 and a smaller peak at 475.1023 *m/z*, in line with the expected masses of $[(phen_2N_2)Fe]^+$ (440.0473 *m/z*) and $[(phen_2N_2)FeCl]^+$ (475.0161 *m/z*), respectively. UV-Vis data also support formation of the metalated complex with a bathochromic shift of the ligand $\pi \rightarrow \pi^*$ transitions and the appearance of shoulders on the main $\pi \rightarrow \pi^*$ peak. Additionally, the ligand peaks at 360 at 376 nm broaden and increase substantially in intensity relative to the main $\pi \rightarrow \pi^*$ peak upon metalation. A new peak appears at 429 nm, while the broad, low-intensity ligand peaks at 439 and 467 nm vanish (Figure S1). The resulting spectrum upon metalation is similar to spectra of tetraaza[14]annulene iron(III) chloride complexes in DMSO.[92]

The ^{57}Fe Mössbauer spectrum of $(phen_2N_2)FeCl$ (Figure 1, middle) reveals a major quadrupole doublet assigned to $(phen_2N_2)FeCl$ and a minor doublet assigned to residual Fe_2Cl_6•$(DMF)_3$.[93,94] The major quadrupole doublet for $(phen_2N_2)FeCl$ is described by $\delta = 0.39$ mm s^{-1} and $|\Delta E_Q| = 3.06$ mm s^{-1}. These parameters are dramatically different from those of (OEP)FeCl, which displays an δ of 0.30 mm s^{-1} and a $|\Delta E_Q|$ of 0.60 mm s^{-1} (Figure S2). The particularly large $|\Delta E_Q|$ observed for $(phen_2N_2)FeCl$ suggests that the iron center exists in an $S = 3/2$ intermediate spin state or an

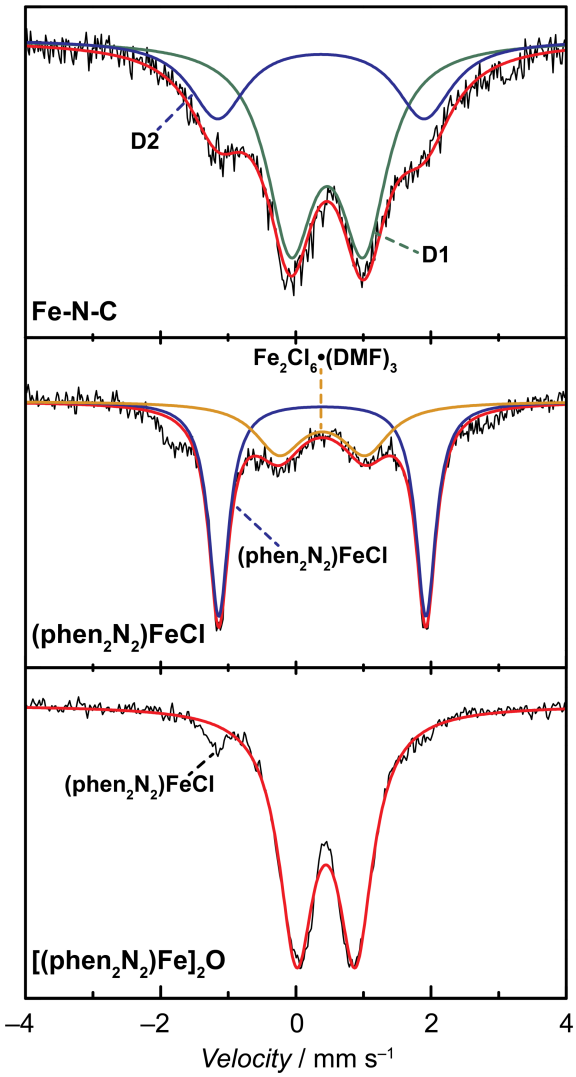

Figure 1. Zero-field ^{57}Fe Mössbauer spectra of Fe-N-C: [D1: ($\delta = 0.46$ mm s^{-1}, $|\Delta E_Q| = 1.08$ mm s^{-1}), D2: ($\delta = 0.37$ mm s^{-1}, $|\Delta E_Q| = 3.06$ mm s^{-1}), top], $(phen_2N_2)FeCl$: [($\delta = 0.39$ mm s^{-1}, $|\Delta E_Q| = 3.06$ mm s^{-1}), middle] and $[(phen_2N_2)Fe]_2O$: [($\delta = 0.45$ mm s^{-1}, $|\Delta E_Q| = 0.87$ mm s^{-1}), bottom] recorded at 90 K. The spectrum of $(phen_2N_2)FeCl$ was fit to two quadrupole doublets assigned to $(phen_2N_2)FeCl$ (blue) and a residual Fe_2Cl_6•$(DMF)_3$ impurity [($\delta = 0.39$ mm s^{-1}, $|\Delta E_Q| = 1.27$ mm s^{-1}), yellow].

$S = 3/2$, 5/2 admixture spin state as has been observed for other iron(III) N_4 macrocycles complexes (Table S2).[49,92,95–106] This assignment is consistent with our calculations on $(phen_2N_2)FeCl$ which predict an intermediate-spin ground state (see SI for details). This electronic structure is consistent with a compressed N_4-binding pocket (see below) that stabilizes the $S = 3/2$ spin state. Although the ^{57}Fe Mössbauer parameters for $(phen_2N_2)FeCl$ are similar to those of the D2 doublet in Fe-N-C, we caution against over-interpreting this similarity because ^{57}Fe Mössbauer spectra are highly sensitive to axial ligation (see below) and the axial Cl in $(phen_2N_2)FeCl$ is distinct from the putative OH_x ligand present in Fe-N-C materials.

To better mimic the axial O-ligation present in the material, we Soxhleted the $(phen_2N_2)FeCl$ sample with ethanol. This served to remove some residual iron salts and generate the μ-oxo $[(phen_2N_2)Fe]_2O$ via reaction with adventitious water and base (see below for XPS and XAS characterization). Similar conversions are well-documented for sterically unprotected porphyrin complexes.[107] While this species is catalytically inactive in acidic electrolyte (Figure S3a),[108,109] it provides a good spectroscopic model for Fe-N-C materials and the analogous $[(OEP)Fe]_2O$ was synthesized by a literature method[107] for comparison.

The ^{57}Fe Mössbauer spectrum of the $[(phen_2N_2)Fe]_2O$ complex is a doublet (Figure 1, bottom), described by $\delta = 0.45$ mm s^{-1} and $|\Delta E_Q| = 0.87$ mm s^{-1}. Our sample of $[(OEP)Fe]_2O$ displays ^{57}Fe Mössbauer parameters of $\delta = 0.41$ mm s^{-1} and $|\Delta E_Q| = 0.67$ mm s^{-1} (Figure S4). Notably, the ^{57}Fe Mössbauer parameters for both $[(OEP)Fe]_2O$ and $[(phen_2N_2)Fe]_2O$ as well as other μ-oxo compounds[101,110] are within the range of values reported for the D1 doublet in Fe-N-C materials. The vast differences in the ^{57}Fe Mössbauer spectra of $(phen_2N_2)Fe$ and (OEP)Fe upon exchange of the axial ligand suggest that ^{57}Fe Mössbauer spectroscopy alone may be insufficient to distinguish pyrrolic from pyridinic ligation at putative $Fe-N_4$ sites in Fe-N-C materials.

XPS of $[(phen_2N_2)Fe]_2O$ Reveals Nitrogen and Iron Environments Similar to Fe-N-C. The nitrogen environments present in Fe-N-C, $[(phen_2N_2)Fe]_2O$, $(phen_2N_2)H_2$ and $[(OEP)Fe]_2O$ were analyzed by X-ray photoelectron spectroscopy (XPS) (see Figures S5–S6 for XPS survey spectra of all compounds and Table S3 for N:Fe ratios of all samples). For Fe-N-C, we observed a broad N 1s XPS signal similar to that reported for other Fe-N-C materials (Figure 2a, top). The N peak envelope for Fe-N-C spans from 396 to 407 eV and can be deconvoluted into four peaks, previously assigned to oxidized (404.0 eV), graphitic/pyrrolic (401.3 eV), metal-coordinated (399.9 eV) and pyridinic nitrogen (398.3 eV).[111,112] Percent nitrogen content is broken down by component in Table S4. We note that since this sample was prepared by pyrolysis of a zinc imidazolate MOF, ZIF-8, we expect the metal-coordinated N peak to result from both iron and zinc coordination. In agreement with our expectations, literature reports[44,45] suggest that the binding energy of the coordinated N peak is largely insensitive to metal identity.

The very broad peak envelope for Fe-N-C contrasts with the well-defined nitrogen environments in $[(OEP)Fe]_2O$ and $[(phen_2N_2)Fe]_2O$. For $[(phen_2N_2)Fe]_2O$, high resolution N 1s spectra (Figure 2a, middle) reveal a single broad peak centered at 399.3 eV that can be deconvoluted into two components centered at 398.3 and 399.6 eV with a peak integration ratio of 1:2. Based on the integration ratio and the symmetry of the $(phen_2N_2)Fe$ subunits in $[(phen_2N_2)Fe]_2O$, we assign the 398.3 peak to the to the bridgehead nitrogens and the 399.6 peak to the coordinated pyridine nitrogens. In comparison, the N 1s XPS spectrum (Figure S7) of $(phen_2N_2)H_2$ is dominated by two peaks corresponding to bridging and pyridinic nitrogen atoms at 397.9 and 399.4 eV, respectively in a 1:2 ratio. This indicates that both bridging and pyridinic nitrogen atoms shift to higher binding energies upon metalation with iron. Similar changes in the N 1s spectrum have been reported for free-base porphyrins upon metalation.[113] In contrast, the XPS N 1s spectrum of $[(OEP)Fe]_2O$ differs markedly from that of $[(phen_2N_2)Fe]_2O$ and consists of a sharp peak at 397.6 eV with a broad satellite peak centered at 400.0 eV[114,115] (Figure 2a, bottom). N 1s peaks for $(phen_2N_2)FeCl$ and (OEP)FeCl (Figure S8) appear within 0.3–0.4 eV of the corresponding peaks for the μ-oxo compounds, indicating that the identity of the axial ligand does not impact the N 1s binding energy to the same extent as does changing the nature of the metal-coordinated nitrogen atoms from pyrrolic to pyridinic. Importantly, the N 1s peak for the coordinated pyridine nitrogens in $(phen_2N_2)Fe$-X complexes matches well with the peak corresponding to the metal-coordinated pyridinic nitrogen component (399.9 eV) of Fe-N-C, whereas the N 1s peak of coordinated pyrrolic nitrogens in (OEP)Fe-X complexes appear at significantly lower binding energies. Together, the XPS data indicate that the iron-coordinated N environment in $[(phen_2N_2)Fe]$ species are electronically very similar to the metal-coordinated N environments in Fe-N-C materials.

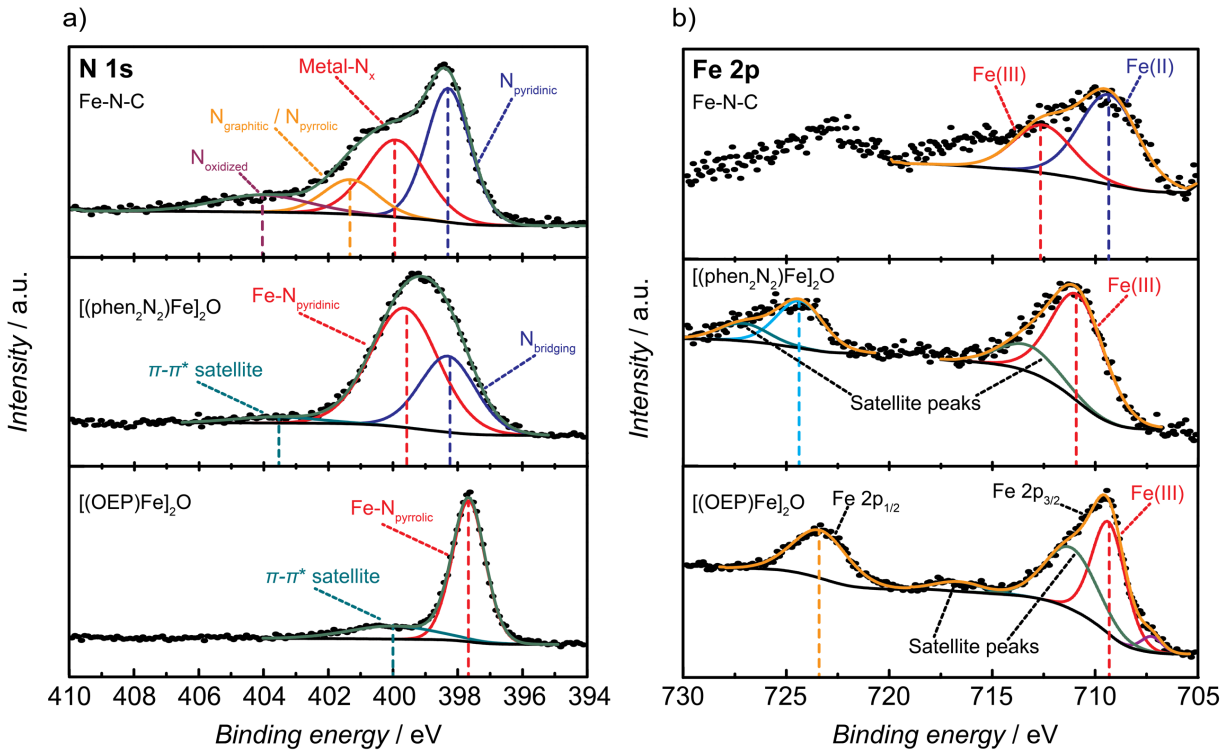

Figure 2. High resolution N 1s (a) and Fe 2p (b) XPS spectra of Fe-N-C (top), $[(phen_2N_2)Fe]_2O$ (middle), and $[(OEP)Fe]_2O$ (bottom).

The iron environments present in Fe-N-C, $[(phen_2N_2)Fe]_2O$ and $[(OEP)Fe]_2O$ were also examined by XPS. Consistent with previously reported data of Fe-N-C materials,[116] we observe Fe $2p_{3/2}$ peaks at 709.8 and 713.5 eV (Figure 2b, top) assigned to Fe(II) and Fe(III) formal oxidation states, respectively (Table S5).[111] In contrast, $[(OEP)Fe]_2O$ (Figure 2b, bottom) displays Fe $2p_{3/2}$ and Fe $2p_{1/2}$ peaks at 709.3 and 723.3 eV, respectively. As reported in the literature for iron porphyrin and phthalocyanine samples, we also observe tailing shoulders on the main Fe $2p_{3/2}$ peak as well as a broad satellite feature that are thought to arise from core-hole interactions with the open-shell electronic structure high-spin ferric centers of $[(OEP)Fe]_2O$.[117,118] Similar features are observed for (OEP)FeCl, albeit with a ~0.7–0.9 eV shift to higher binding energy (Figure S9). These XPS features are distinct from those observed for $[(phen_2N_2)Fe]_2O$ (Figure 2b, middle) which displays Fe $2p_{3/2}$ and $2p_{1/2}$ peaks at 710.8 and 724.3 eV. We note that $(phen_2N_2)FeCl$ shows Fe $2p_{3/2}$ and $2p_{1/2}$ peaks at similar binding energies, 710.8 and 724.7 eV, respectively (Figure S10), and that residual $FeCl_3$ salts are likely to be subsumed into these peaks.[119] As with $[(OEP)Fe]_2O$, we also observe a higher binding energy satellite on the main Fe $2p_{3/2}$ peak of $[(phen_2N_2)Fe]_2O$ that we also attribute to core-hole interactions with an open-shell ferric center. There is some asymmetry to the Fe $2p_{1/2}$ peak which likely originates from the same effect. Importantly, we observe a ~1.5 eV shift to higher binding energy for the main Fe $2p_{3/2}$ peak for $[(phen_2N_2)Fe]_2O$ relative to that in $[(OEP)Fe]_2O$. This observation is consistent with increased π-acidity of the pyridinic macrocycle in $[(phen_2N_2)Fe]_2O$, which withdraws electron density from the iron center. Notably, the peak in Fe-N-C previously assigned to Fe(III) is 2.7 eV positive of the corresponding Fe(III) peak for $[(phen_2N_2)Fe]_2O$ but even more positive than the same peak in $[(OEP)Fe]_2O$. These data suggest that while the Fe(III) centers in Fe-N-C may exist in an even more withdrawing ligation environment, a pyridinic macrocycle complex such as $[(phen_2N_2)Fe]_2O$ provides a better structural model for Fe-N-C than a porphyrin complex such as $[(OEP)Fe]_2O$. Indeed, the strongly electron withdrawing environment in the material helps to explain the positive shift of the putative Fe(II) component of Fe-N-C, which makes it appear close in energy to the main Fe $2p_{3/2}$ peaks for both of the Fe(III) complexes examined here. Taken as a whole, the XPS data are consistent with nitrogen and iron environments in $[(phen_2N_2)Fe]_2O$ that are more electropositive than a typical metalloporphyrin and more similar to the metal-N_x sites in Fe-N-C.

XAS Results Demonstrate A Strong Resemblance Between Fe-N-C and $[(phen_2N_2)Fe]_2O$. We next examined the electronic structure and coordination environment of the iron centers in Fe-N-C, $[(phen_2N_2)Fe]_2O$, and $[(OEP)Fe]_2O$ by X-ray absorption spectroscopy (XAS). The XANES spectrum of our Fe-N-C preparation (Figure 3a, black) matches

those reported in the literature.[33] While a rigorous analysis of the X-ray absorption near edge structure (XANES) spectra for Fe-N-C materials is challenging due to the presumed presence of a mixture of Fe(II) and Fe(III) (Table S5) as well as an unknown degree of heterogeneity in the local coordination environment of each

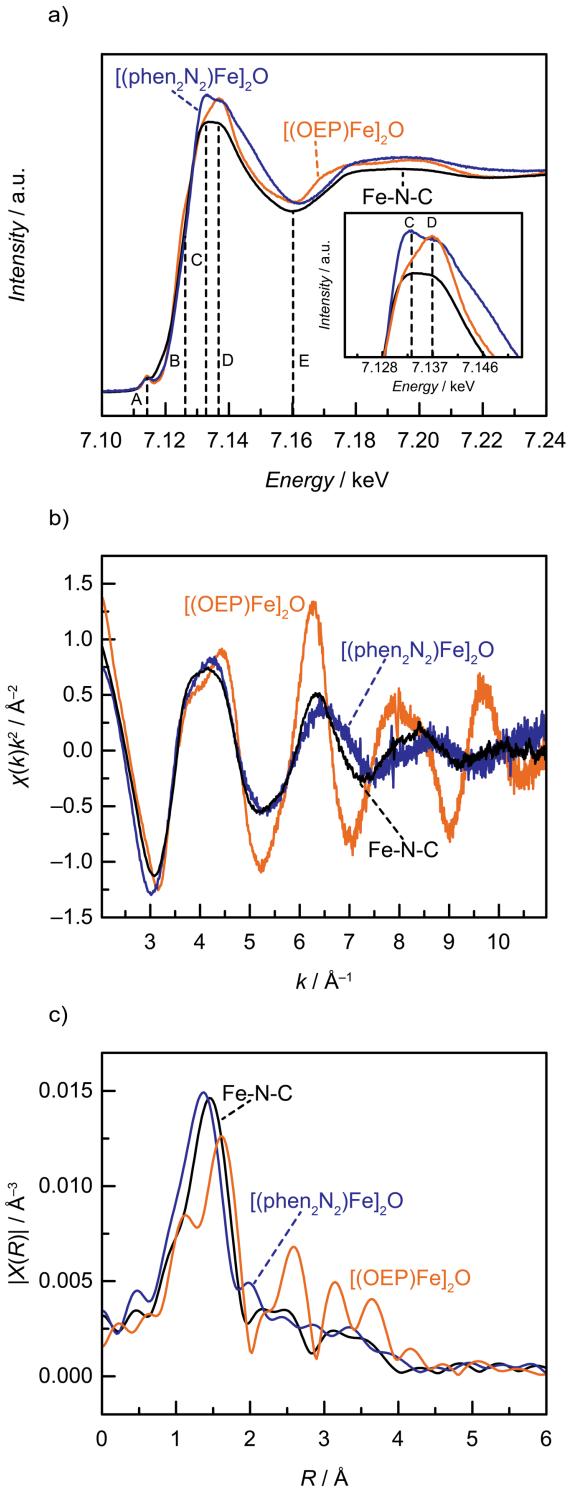

Figure 3. X-ray absorption spectroscopy data for Fe-N-C (black), $[(phen_2N_2)Fe]_2O$ (blue), and $[(OEP)Fe]_2O$ (orange). XANES spectra (a) and expanded main-edge region (inset), k^2-weighted Fe k-edge EXAFS spectra (b) and k^2-weighted Fourier transform Fe EXAFS spectra (c). The energy values of the vertical lines and the alphabetical labels in (a) are taken from reference 33.

iron, the XANES line shapes have been exhaustively examined for a wide variety of pyrolyzed Fe-N-C catalysts and features of the XANES have been correlated to ORR activity.[33,34,120] In particular, the intensity of the first main edge peak, C, has been found to positively correlate with ORR activity, whereas the intensities of the main edge shoulder, B, and the higher energy main edge peak, D, have been shown to anticorrelate with ORR activity (Figures 3a, dotted vertical lines). Notably, whereas the XANES spectra of $[(OEP)Fe]_2O$ (Figure 3a, orange) shows enhanced intensity for B and D, the XANES spectra of $[(phen_2N_2)Fe]_2O$ (Figure 3a, blue) shows a higher intensity for C, and lower intensities for B and D. The intensity of pre-edge peak, A, has also been shown to positively correlate with ORR activity.[33] We find that the pre-edge peak line shape for $[(phen_2N_2)Fe]_2O$ matches closely with that of Fe-N-C, but that the peak intensity for both is lower than that for $[(OEP)Fe]_2O$ (Figure S11). Given the high sensitivity of the pre-edge peak to the identity of the axial ligand in similar porphyrinoid complexes[121] as well as distortions in the $Fe-N_4$ plane made possible by variation of the Fe-O-Fe angle in $[(OEP)Fe]_2O$,[107,122] we refrain from over-interpreting the pre-edge peak shapes or intensity.[123] Nonetheless, the suppressed intensity at B and D and increased intensity at C for $[(phen_2N_2)Fe]_2O$ suggests that the $(phen_2N_2)Fe$ molecular analogue is a superior model for the active sites in Fe-N-C materials relative to (OEP)Fe.

Extended X-ray absorption fine structure (EXAFS) data provide further evidence in support of the structural similarity between the iron coordination environments in $[(phen_2N_2)Fe]_2O$ and Fe-N-C. The k^2-weighted EXAFS oscillations for Fe-N-C (Figure 3b, black) exhibit remarkably similar amplitudes and periods to the EXAFS of $[(phen_2N_2)Fe]_2O$ (Figure 3b, blue) out to ~10.0 $Å^{-1}$ with only a small phase shift beyond ~6.0 $Å^{-1}$. In contrast, the k^2-weighted EXAFS for $[(OEP)Fe]_2O$ (Figure 3b, orange) displays amplitudes and periods that differ dramatically from the EXAFS of $[(phen_2N_2)Fe]_2O$ and Fe-N-C beyond ~4.0 $Å^{-1}$.

The striking similarity between Fe-N-C and $[(phen_2N_2)Fe]_2O$ is also reflected in the k^2-weighted Fourier transform EXAFS radial distribution spectra (Figure 3c). In particular, the $[(phen_2N_2)Fe]_2O$ complex displays a primary coordination shell scattering peak at 1.36 Å apparent distance, similar to the first shell peak for Fe-N-C at 1.46 Å apparent distance. In contrast, the first shell scattering peak for $[(OEP)Fe]_2O$ appears at 1.62 Å apparent distance. The first shell EXAFS peaks for all three materials are well modeled with a five-coordinate Fe center bearing four equatorial Fe-N scatterers and one axial Fe-O scatterer (Table S6). The fits (Figure S12) from modeling the data return Fe-N scattering paths of 1.94, 1.97, and 2.06 Å for Fe-N-C, $[(phen_2N_2)Fe]_2O$, and $[(OEP)Fe]_2O$, respectively. The 2.06 Å value for $[(OEP)Fe]_2O$ is in line with crystal structure data showing an average Fe–N bond distance of 2.08 Å.[107] For $[(phen_2N_2)Fe]_2O$, the 1.97 Å distance extracted from EXAFS modeling (Table S6 and Figure S12) is substantially higher than the 1.86 Å distance predicted from calculation if the Fe were to reside in the N_4 plane for the $phen_2N_2$ ligand (Figure S13). Instead, the EXAFS data suggest that the Fe sites are puckered out of the $Fe-N_4$ plane and that a similar phenomenon may exist for Fe sites in Fe-N-C materials. Indeed, a computational XAS study showed an enhancement of the main edge peak C as the displacement of Fe from the N_4 plane was increased.[33] Consistent with the Fe-N-C material having a putative OH_x axial ligand, the EXAFS fits return a Fe-O scattering path of 2.04 Å, slightly larger than the Fe-O scattering path of 1.79 Å extracted for both molecular μ-oxo complexes. For $[(OEP)Fe]_2O$, we also observe higher shell scatter peaks that could arise from a long-range Fe-Fe scattering pathway across the μ-oxo linkage. These so-called focusing effect peaks are highly sensitive the Fe-O-Fe angle and so deviations from 180° could contribute to the attenuation of this peak for $[(phen_2N_2)Fe]_2O$. In aggregate, the EXAFS data highlight the compressed primary coordination environment observed for both Fe-N-C and $[(phen_2N_2)Fe]_2O$ relative to $[(OEP)Fe]_2O$, further bolstering the notion that $[(phen_2N_2)Fe]_2O$ closely models the active sites in F-N-C materials.

$(Phen_2N_2)Fe$ Displays an Fe(III/II) Redox Potential Higher than (OEP)Fe and More Similar to Fe-N-C. Both model compounds and the Fe-N-C material were evaluated electrochemically as thin films supported on glassy carbon electrodes. In a typical preparation, Fe-N-C powders were dispersed in a 7:2:1 combination of CH_2Cl_2, ethanol, and 5 wt% Nafion solution (75 wt% ethanol and 20 wt% water), respectively. The resulting inks were dropcast onto a glassy carbon disk electrode and allowed to dry in air to generate a well-adhered catalyst film. A similar procedure was used for $(phen_2N_2)FeCl$ and (OEP)FeCl with inclusion of Vulcan carbon powder to enhance film conductivity (see the Supporting Information for details of film preparation and characterization, Table S7). We expect that any residual $FeCl_3$ salts present in the $(phen_2N_2)FeCl$ sample will readily dissolve into the acidic electrolyte and will, therefore, not impact the electrochemical results. In line with this expectation, we find that $FeCl_3$/Vulcan inks are inactive for ORR (Figure S14).

Cyclic voltammograms of Fe-N-C, ($phen_2N_2$)FeCl, and (OEP)FeCl recorded in the absence of O_2 provide insight into the redox potential of the metal center. For (OEP)Fe (Figure 4, orange), we observe a broad redox feature with $E_{1/2}$ = 0.27 V (all potentials are reported vs the reversible hydrogen electrode, RHE), similar to reported values for carbon-supported iron porphyrin complexes.[108,124] For ($phen_2N_2$)Fe (Figure 4, blue), we observe a reversible redox wave at 0.59 V. Based on the known Nernstian pH dependence of Fe(III/II) couples for adsorbed porphyrin complexes[125] as well as the quasi-Nernstian behavior of the redox wave for ($phen_2N_2$)Fe (Figure S15), we assign these redox processes to the one-electron, one-proton reduction of Fe(III)-OH to Fe(II)-OH_2. For Fe-N-C (Figure 4, black),

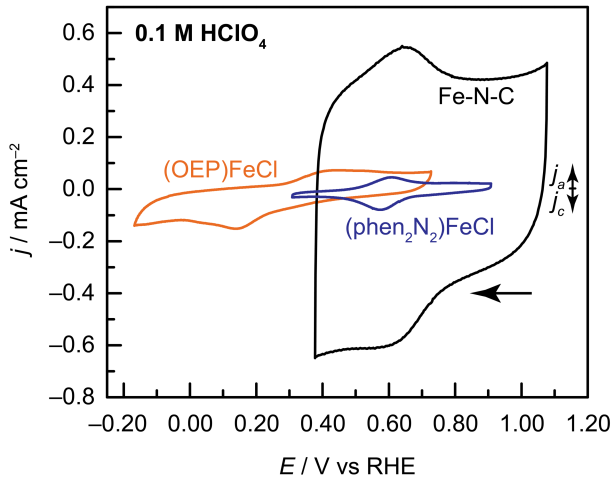

Figure 4. Cyclic voltammograms of rotating glassy carbon disk electrodes modified with catalyst films containing Fe-N-C (black), ($phen_2N_2$)FeCl (blue), and (OEP)FeCl (orange). Data were recorded at 5 mV s^{-1} and 2000 rpm rotation rate in O_2-free 0.1 M $HClO_4$ electrolyte.

we observe a large double layer capacitance, consistent with the high surface area of the material, and a pronounced redox wave at 0.63 V (Figure 4). Other literature reports have observed waves for Fe-N-C materials at ~0.8 V,[126,127] in line with the onset of ORR catalysis at Fe-N-C materials (see below) and so we attribute the wave we observe at 0.63 V to proton-coupled electron transfer (PCET) reactions of quinone and hydroxyl moieties on the Fe-N-C surface.[128] We postulate that the actual Fe(III)-OH/Fe(II)-OH_2 redox process for Fe-N-C is obscured by the large double layer charging background in this high surface area material and the likely distribution of iron redox potentials in the heterogeneous material. We also note that some Fe redox centers may not engage in PCET reactivity and would, therefore, not be expected to display a redox wave.[129] Nonetheless, the 0.32 V positive shift of the Fe redox couple for ($phen_2N_2$)Fe vs (OEP)Fe is consistent with the more electron withdrawing character of the pyridinic primary ligation sphere, which brings this model complex much closer in electronic character to the electropositive iron environments in Fe-N-C materials.

The observed Fe(III/II) redox waves result from only a fraction of the catalyst loaded into the dropcast film. The integrated charge in the Fe(III/II) redox waves of the ($phen_2N_2$)FeCl catalyst film corresponds to 7% of the total catalyst loading (Table S7). This contrasts with the (OEP)FeCl film, for which the Fe(III/II) wave integration corresponds to 43% of the total catalyst loading. We attribute this difference to the improved solubility of the porphyrin catalyst leading to better dispersion within the film. Nonetheless, these PCET redox potentials provide a good indication that the iron centers in ($phen_2N_2$)Fe are more electropositive than those in (OEP)Fe.

($Phen_2N_2$)FeCl Catalyzes ORR at Lower Overpotentials and with Higher TOF Values than (OEP)FeCl. ($Phen_2N_2$)FeCl is a potent catalyst for the oxygen reduction reaction. In O_2-saturated 0.1 M $HClO_4$, the reversible surface redox wave at 0.59 V (Figure 5, black) is replaced by a large catalytic wave that displays an onset potential of 0.75 V (all onset potentials correspond to a current density of 0.1 mA cm^{-2} and all electrochemical performance parameters are collected in Table S8) and reaches a current plateau at ~0.5 V (Figure 5, red). This catalytic wave spans the same potential range as the reversible redox feature in the absence of O_2 suggesting that ORR catalysis is mediated by the Fe(III/II) redox process (Figure 5, inset). Catalytic activity is improved in basic media with an onset of 0.88 V in 0.1 M KOH (Figure S14a). The catalytic activity of ($phen_2N_2$)FeCl (Figure 6, blue) is significantly greater than that

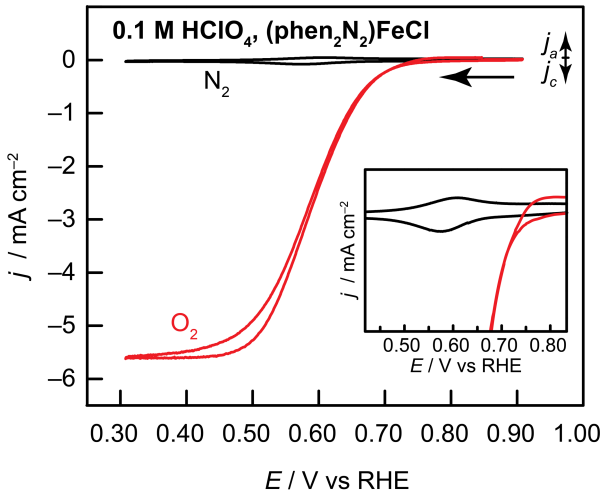

Figure 5. Cyclic voltammograms of a rotating glassy carbon disk electrode modified with a catalyst film containing $(phen_2N_2)FeCl$ in N_2- (black) and O_2- (red) saturated 0.1 M $HClO_4$ aqueous electrolyte. Data were recorded at 5 mV s^{-1} and 2000 rpm rotation rate.

of (OEP)FeCl (Figure 6, orange), which displays onset potentials of 0.45 and 0.74 V in $HClO_4$ and KOH, respectively. Additionally, the unmetalated $(phen_2N_2)H_2$ ligand has activity comparable to the carbon background (Figure 6, green) in acidic media with an onset potential of 0.34 V (Figure 6, red) and activity slightly higher than background in alkaline media with an onset potential of 0.75 V (Figures S16a and S17). Notably, the 0.3 V increase in ORR onset potential for $(phen_2N_2)FeCl$ relative to (OEP)FeCl in acid is comparable to the 0.32 V positive shift in the Fe(III/II) redox potential. For homogeneous molecular iron porphyrins, TOF values typically track inversely with the Fe(III/II) redox potential. Yet, for $(phen_2N_2)FeCl$, the dramatic increase in Fe(III/II) potential does not seem to lead to a correlated decrease in ORR rate[72] suggesting that $(phen_2N_2)FeCl$ does not follow the same linear free-energy correlations observed for molecular porphyrin catalysts. The catalytic enhancement is also reflected in significantly

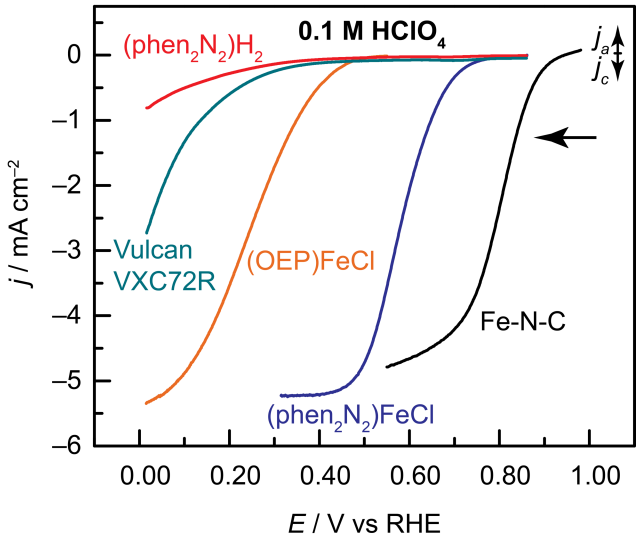

Figure 6. Linear sweep voltammograms of glassy carbon disk electrodes modified with catalyst films containing Fe-N-C (black), $(phen_2N_2)FeCl$ (blue), (OEP)FeCl (orange), Vulcan carbon (green), and $(phen_2N_2)H_2$ (red) in O_2-saturated 0.1 M $HClO_4$ electrolyte. Data were recorded at 5 mV s^{-1} and 2000 rpm rotation rate.

increased per-site turnover frequencies (TOFs). TOF values in electron passed per site per second were extracted as a function of potential by dividing the current density by the integrated charge passed in the Fe(III/II) redox feature

(Figures 7a and S16b). Remarkably, ($phen_2N_2$)FeCl displays a dramatically enhanced TOF that is 1400-fold higher than that of (OEP)FeCl in the activation-controlled region at 0.55 V in 0.1 M $HClO_4$ and 230-fold higher in the same region at 0.80 V in 0.1 M NaOH (Table S9). These observations establish that changing the primary coordination environment from pyrrolic to pyridinic leads to a dramatic enhancement in catalytic activity for ORR.

Although the catalytic performance of ($phen_2N_2$)FeCl is superior to (OEP)FeCl, it remains at a deficit to Fe-N-C. While the Fe(III/II) redox potential is difficult to discern for Fe-N-C, the positive shift of the Fe(III) peak in the XPS suggest that the iron centers in Fe-N-C are even more electropositive than the those in ($phen_2N_2$)FeCl and this may contribute to the higher onset potential of 0.90 V for the Fe-N-C catalyst (Figure 6, black).[17] Furthermore, unlike in ($phen_2N_2$)FeCl, the iron centers in Fe-N-C interact strongly with the delocalized band states of the N-doped graphitic carbon matrix and, indeed, a recent study on cobalt porphyrins indicates that strong electron coupling to graphite can dramatically increase ORR activity relative to a porphyrin of identical local structure with weak coupling to the surface.[130] Studies are ongoing to synthesize ($phen_2N_2$)FeCl analogs that can be conjugated to graphitic carbon electrodes to directly examine the role of electronic coupling on ORR activity. Notwithstanding, the fact that a discrete molecular complex such as ($phen_2N_2$)FeCl displays an ORR onset within 150 mV of champion Fe-N-C materials suggests enormous opportunities for rational molecular design of highly active Fe-based ORR catalysts based upon pyridinic macrocyclic complexes.

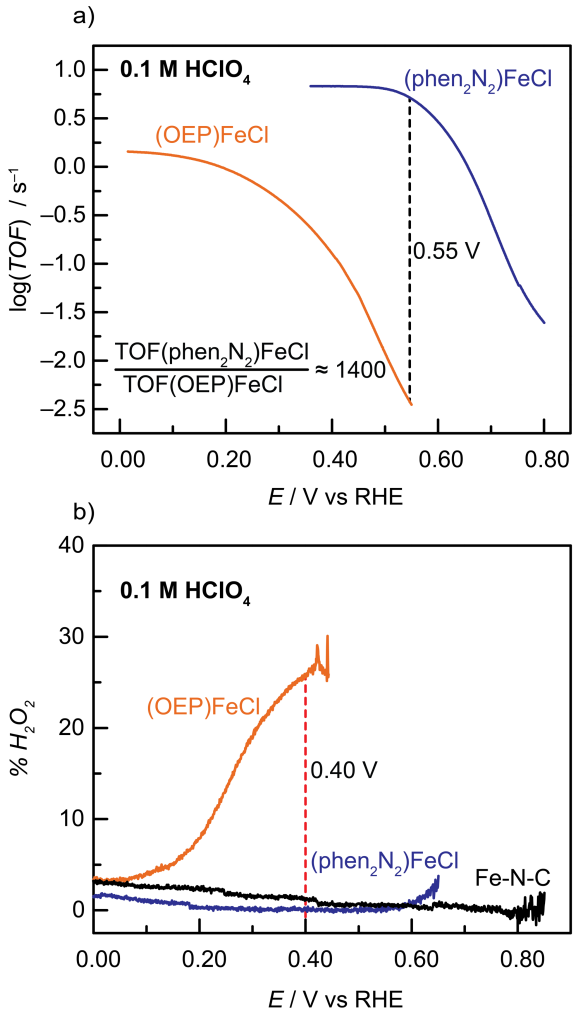

Figure 7. Log(TOF) for ORR vs potential (a) for ($phen_2N_2$)FeCl (blue) and (OEP)FeCl (orange). $\%H_2O_2$ vs potential (b) for ($phen_2N_2$)FeCl (blue), (OEP)FeCl (orange) and Fe-N-C (black). All data were recorded in O_2-saturated 0.1 M $HClO_4$ electrolyte at 5 mV s^{-1} and 2000 rpm rotation rate.

Furthermore, ($phen_2N_2$)FeCl displays high selectivity for the four-electron reduction of O_2 that is comparable to Fe-N-C and greater than that of (OEP)FeCl. Using rotating ring disk electrode (RRDE) voltammetry (Figures S18 and S19) we determined the percent H_2O_2 produced as a function of applied potential for all three catalysts (Figure 7b and S18). For ($phen_2N_2$)FeCl, H_2O_2 production stabilizes rapidly, reaching values of <1% and 3% in acid and alkaline media at 0.40 V vs RHE, respectively (Figures 7b and S20, blue).These values correspond to 3.99 and 3.95 electrons transferred in each condition, respectively, (Figure S21). Indeed, in both acidic and alkaline media, the selectivity of ($phen_2N_2$)FeCl in the transport-limited region surpasses that of Fe-N-C at the same potential (1% and 5% H_2O_2 in 0.1 M $HClO_4$ and 0.1 M NaOH, respectively, at 0.40 V). Further, in stark contrast to ($phen_2N_2$)FeCl, (OEP)FeCl displays significantly lower selectivity with 26% and 4% H_2O_2 in acidic and alkaline media, respectively, at the same potential of 0.40 V (Figures 7b and S20, orange). Notably, for all catalysts examined, the hydrogen peroxide percentages increase in alkaline media and this may result from the action of less-selective non-metallic active sites capable of ORR in alkaline media.[131–134] Indeed, for the metal-free ($phen_2N_2$)H_2 ligand supported on carbon, we observed significantly higher levels of H_2O_2 in alkaline media (17% at 0.40 V and a maximum of 26%, Figure S22b). Overall, these results highlight the ability of this tetrapyridinic Fe-N_4 coordination environment to facilitate selective O_2-reduction pathways in both acidic and alkaline media. The similar trends in selectivity between this complex and Fe-N-C further support the notion that the ($phen_2N_2$)Fe motif is an effective functional model of Fe-N-C catalysts.

Whereas Fe-N-C materials are relatively stable, we observe limited stability of the ($phen_2N_2$)FeCl catalyst with activity decaying in acidic media over the course of several slow scan cyclic voltammograms (15–20 min). A similar deactivation is also observed for (OEP)FeCl and is well-documented in the literature.[135–137] These observations highlight the important role of the carbon framework in increasing the relative stability of Fe-N_4 sites in Fe-N-C materials against oxidative and protolytic decomposition induced by the acidic conditions and the presence of parasitic amounts of H_2O_2.[138] Indeed, we posit that extending the aromatic periphery around the ($phen_2N_2$)FeCl active site could enhance stability and provide a path towards the bottom-up synthesis of robust Fe-based ORR catalysts.

CONCLUSIONS

The results reported herein provide a molecular perspective on the structure and oxygen reduction reactivity of Fe-N_4 active sites in Fe-N-C materials. We have demonstrated that ($phen_2N_2$)Fe fragments are superior molecular models of the putative Fe-N_4 active sites in Fe-N-C materials than the exhaustively studied iron porphyrin complexes. The pyridinic ligation environment in ($phen_2N_2$)Fe leads to XPS and XAS signatures that are remarkably similar to those of Fe-N-C materials. Furthermore, pyridinic ligation leads to a more electropositive metal center that shifts the onset potential of ORR catalysis to 300 mV lower overpotential and leads to TOF values 1400-fold higher than that of (OEP)Fe. The ($phen_2N_2$)Fe platform displays this rate enhancement while also dramatically improving selectivity for four-electron oxygen reduction to near 100%. Considering both activity and selectivity, ($phen_2N_2$)Fe is, to the best of our knowledge, the highest performing molecular Fe-based ORR catalyst ever reported in acidic media and its performance closely approaches that of champion Fe-N-C materials that have been optimized over many decades.

By developing a high fidelity structural and functional model of the active sites in Fe-N-C, our work enables the discovery of new structure-spectroscopy-activity correlations that would be impossible to extract from studies of pyrolyzed Fe-N-C materials alone. In particular, the ($phen_2N_2$)Fe core can be readily derivatized to vary the metal identity,[79] the axial ligand, the in-plane ligating atom, the bridgehead atom[139,140] and the substitution pattern of each phenanthroline moiety. This provides a diverse family of compounds for spectroscopic comparison to Fe-N-C materials, improving the understanding of active site structure in this important class of catalysts.

The ($phen_2N_2$)Fe core developed here also allows for rational design of improved ORR catalysts. Unlike for Fe-N-C materials, synthetic derivatization of the ($phen_2N_2$)Fe architecture will uniformly modify all the active sites in the material, allowing for the extraction of molecular-level free-energy correlations. Moreover, borrowing from extensive studies of molecular porphyrin complexes,[141–148] the secondary coordination sphere around the ($phen_2N_2$)Fe core can be tuned to generate three-dimensional surface active site environments that would be impossible to synthesize faithfully and selectively by traditional pyrolysis methods. Integration of the ($phen_2N_2$)Fe motif within metal-organic frameworks[149] or other porous polymers[150] provides a route for accessing a new generation of Fe-N-C materials with high active site densities inaccessible by pyrolysis. Thus, the molecular model complex developed here provides a powerful platform with which to advance the synthesis and understanding of single-site heterogeneous electrocatalysts for critical energy conversation reactions.

METHODS

Full experimental details and methods are listed in the SI. Synthesis and characterization of all complexes and precursor compounds, ink preparation, XAS fitting parameters and errors, electronic structure calculations and electrochemical controls are given in the SI.

DATA AVAILABILITY

Data generated or analysed during this study are included in this article and/or its supplementary information files. Raw data are available from the authors on request.

AUTHOR CONTRIBUTIONS

Y.S. and T.M.-R. conceived of the research. T.M.-R. synthesized all compounds and catalysts, collected all XPS and electrochemical data and analysed all spectroscopic and electrochemical results. N.J.L. and J.T.M. collected and analysed the XAS data. A.T.W. and K.J.A. collected and analysed the Mössbauer spectra. N.D.R. and T.V.V. performed computations. Y.S. assisted with experimental design and data analysis. T.M.-R and Y.S. wrote the manuscript with input from all authors.

ACKNOWLEDGEMENT

This research was primarily supported as part of the Center for Molecular Electrocatalysis, an Energy Frontier Research Center funded by the U.S. Department of Energy (DOE), Office of Science, Basic Energy Sciences (BES). The computational work was supported by a seed grant from the MIT Energy Initiative. T. M.-R. acknowledges the Department of Defense (DoD) for a National Defense Science & Engineering Graduate Fellowship (NDSEG). Use of the Advanced Photon Source is supported by the U.S. Department of Energy, Office of Science, and Office of Basic Energy Sciences, under Contract DE-AC02-06CH11357. MRCAT operations are supported by the Department of Energy and the MRCAT member institutions. XPS investigations were performed at the Center for Nanoscale Systems (CNS), a member of the National Nanotechnology Coordinated Infrastructure Network (NNCI), which is supported by the National Science Foundation under NSF award no. 1541959. CNS is a part of Harvard University. Y.S. acknowledges the Sloan Foundation, Research Corporation for Science Advancement (Cottrell Scholar), and the Canadian Institute for Advanced Research (CIFAR Azrieli Global Scholar).

MATERIALS AND CORRESPONDENCE

*yogi@mit.edu

COMPETING INTERESTS

The authors declare the following competing financial interest(s): T.M.-R and Y.S. are inventors on patent application 62/818,284, submitted by the Massachusetts Institute of Technology, that covers the hexaazamacrocycle iron complex and related catalyst ink described in this work.

REFERENCES

1. Seh, Z. W. *et al.* Combining theory and experiment in electrocatalysis: insights into materials design. *Science* **355**, eaad4998 (2017).
2. Winter, M. & Brodd, R. J. What are batteries, fuel cells, and supercapacitors? *Chem. Rev.* **104**, 4245–4270 (2004).
3. Shao, M., Chang, Q., Dodelet, J.-P. & Chenitz, R. Recent advances in electrocatalysts for oxygen reduction reaction. *Chem. Rev.* **116**, 3594–3657 (2016).
4. Sealy, C. The problem with platinum. *Mater. Today* **11**, 65–68 (2008).
5. Steele, B. C. H. & Heinzel, A. Materials for fuel-cell technologies. *Nature* **414**, 345–352 (2001).
6. Gasteiger, H. A., Kocha, S. S., Sompalli, B. & Wagner, F. T. Activity benchmarks and requirements for Pt, Pt-alloy, and non-Pt oxygen reduction catalysts for PEMFCs. *Appl. Catal. B Environ.* **56**, 9–35 (2005).
7. Kinumoto, T. *et al.* Stability of Pt-catalyzed highly oriented pyrolytic graphite against hydrogen peroxide in acid solution. *J. Electrochem. Soc.* **153**, A58–A63 (2006).

8. Ramaswamy, N., Hakim, N. & Mukerjee, S. Degradation mechanism study of perfluorinated proton exchange membrane under fuel cell operating conditions. *Electrochim. Acta* **53**, 3279–3295 (2008).
9. Sethuraman, V. A., Weidner, J. W., Haug, A. T., Motupally, S. & Protsailo, L. V. Hydrogen peroxide formation rates in a PEMFC anode and cathode. *J. Electrochem. Soc.* **155**, B50–B57 (2008).
10. Wu, G. *et al.* Performance durability of polyaniline-derived non-precious cathode catalysts. *ECS Trans.* **25**, 1299–1311 (2009).
11. Jasinski, R. A new fuel cell cathode catalyst. *Nature* **201**, 1212–1213 (1964).
12. Jasinski, R. Cobalt phthalocyanine as a fuel cell cathode. *J. Electrochem. Soc.* **112**, 526–528 (1965).
13. Jaouen, F. *et al.* Toward platinum group metal-free catalysts for hydrogen/air proton-exchange membrane fuel cells. *Johns. Matthey Technol. Rev.* **62**, 231–255 (2018).
14. Lefèvre, M., Proietti, E., Jaouen, F. & Dodelet, J.-P. Iron-based catalysts with improved oxygen reduction activity in polymer electrolyte fuel cells. *Science* **324**, 71–74 (2009).
15. Liu, W. *et al.* Discriminating catalytically active FeN_x species of atomically dispersed Fe–N–C catalyst for selective oxidation of the C–H bond. *J. Am. Chem. Soc.* **139**, 10790–10798 (2017).
16. Kramm, U. I. *et al.* Structure of the catalytic sites in Fe/N/C-catalysts for O_2-reduction in PEM fuel cells. *Phys. Chem. Chem. Phys.* **14**, 11673–11688 (2012).
17. Bouwkamp-Wijnoltz, A. L. *et al.* On active-site heterogeneity in pyrolyzed carbon-supported iron porphyrin catalysts for the electrochemical reduction of oxygen: an *in situ* Mössbauer study. *J. Phys. Chem. B* **106**, 12993–13001 (2002).
18. Faubert, G. *et al.* Iron catalysts prepared by high-temperature pyrolysis of tetraphenylporphyrins adsorbed on carbon black for oxygen reduction in polymer electrolyte fuel cells. *Electrochim. Acta* **43**, 341–353 (1998).
19. Bron, M., Radnik, J., Fieber-Erdmann, M., Bogdanoff, P. & Fiechter, S. EXAFS, XPS and electrochemical studies on oxygen reduction catalysts obtained by heat treatment of iron phenanthroline complexes supported on high surface area carbon black. *J. Electroanal. Chem.* **535**, 113–119 (2002).
20. Zitolo, A. *et al.* Identification of catalytic sites for oxygen reduction in iron- and nitrogen-doped graphene materials. *Nat. Mater.* **14**, 937–942 (2015).
21. Kramm, U. I., Lefèvre, M., Bogdanoff, P., Schmeißer, D. & Dodelet, J.-P. Analyzing structural changes of Fe–N–C cathode catalysts in PEM fuel cell by Mößbauer spectroscopy of complete membrane electrode assemblies. *J. Phys. Chem. Lett.* **5**, 3750–3756 (2014).
22. Jaouen, F., Marcotte, S., Dodelet, J.-P. & Lindbergh, G. Oxygen reduction catalysts for polymer electrolyte fuel cells from the pyrolysis of iron acetate adsorbed on various carbon supports. *J. Phys. Chem. B* **107**, 1376–1386 (2003).
23. Maldonado, S. & Stevenson, K. J. Direct preparation of carbon nanofiber electrodes via pyrolysis of iron(ii) phthalocyanine: electrocatalytic aspects for oxygen reduction. *J. Phys. Chem. B* **108**, 11375–11383 (2004).
24. Kramm, U. I., Lefèvre, M., Larouche, N., Schmeisser, D. & Dodelet, J.-P. Correlations between mass activity and physicochemical properties of Fe/N/C catalysts for the ORR in PEM fuel cell via ^{57}Fe Mössbauer spectroscopy and other techniques. *J. Am. Chem. Soc.* **136**, 978–985 (2014).
25. Rauf, M. *et al.* Insight into the different ORR catalytic activity of Fe/N/C between acidic and alkaline media: protonation of pyridinic nitrogen. *Electrochem. Commun.* **73**, 71–74 (2016).
26. Dodelet, J.-P. The controversial role of the metal in Fe- or Co-based electrocatalysts for the oxygen reduction reaction in acid medium. in *Electrocatalysis in Fuel Cells* (ed. Shao, M.) vol. 9 271–338 (Springer London, 2013).
27. Holst-Olesen, K., Silvioli, L., Rossmeisl, J. & Arenz, M. Enhanced oxygen reduction reaction on Fe/N/C catalyst in acetate buffer electrolyte. *ACS Catal.* **9**, 3082–3089 (2019).
28. Leonard, N. D. *et al.* Deconvolution of utilization, site density, and turnover frequency of Fe–nitrogen–carbon oxygen reduction reaction catalysts prepared with secondary N-precursors. *ACS Catal.* **8**, 1640–1647 (2018).
29. Strickland, K. *et al.* Highly active oxygen reduction non-platinum group metal electrocatalyst without direct metal–nitrogen coordination. *Nat. Commun.* **6**, 7343 (2015).
30. Varnell, J. A. *et al.* Identification of carbon-encapsulated iron nanoparticles as active species in non-precious metal oxygen reduction catalysts. *Nat. Commun.* **7**, 12582 (2016).
31. Ramaswamy, N., Tylus, U., Jia, Q. & Mukerjee, S. Activity descriptor identification for oxygen reduction on nonprecious electrocatalysts: linking surface science to coordination chemistry. *J. Am. Chem. Soc.* **135**, 15443–15449 (2013).
32. Tylus, U. *et al.* Elucidating oxygen reduction active sites in pyrolyzed metal–nitrogen coordinated non-precious-metal electrocatalyst systems. *J. Phys. Chem. C* **118**, 8999–9008 (2014).

33. Jia, Q. *et al.* Experimental observation of redox-induced Fe–N switching behavior as a determinant role for oxygen reduction activity. *ACS Nano* **9**, 12496–12505 (2015).
34. Jia, Q. *et al.* Spectroscopic insights into the nature of active sites in iron–nitrogen–carbon electrocatalysts for oxygen reduction in acid. *Nano Energy* **29**, 65–82 (2016).
35. Gewirth, A. A., Varnell, J. A. & DiAscro, A. M. Nonprecious metal catalysts for oxygen reduction in heterogeneous aqueous systems. *Chem. Rev.* **118**, 2313–2339 (2018).
36. Xiao, M. *et al.* Microporous framework induced synthesis of single-atom dispersed Fe-N-C acidic ORR catalyst and its *in situ* reduced Fe-N_4 active site identification revealed by X-ray absorption spectroscopy. *ACS Catal.* **8**, 2824–2832 (2018).
37. Sahraie, N. R. *et al.* Quantifying the density and utilization of active sites in non-precious metal oxygen electroreduction catalysts. *Nat. Commun.* **6**, 8618 (2015).
38. Luo, F. *et al.* Accurate evaluation of active-site density (SD) and turnover frequency (TOF) of PGM-free metal–nitrogen-doped carbon (MNC) electrocatalysts using CO cryo adsorption. *ACS Catal.* **9**, 4841–4852 (2019).
39. Glibin, V. P. & Dodelet, J.-P. Thermodynamic stability in acid media of FeN_4-based catalytic sites used for the reaction of oxygen reduction in PEM fuel cells. *J. Electrochem. Soc.* **164**, F948–F957 (2017).
40. Lefèvre, M., Dodelet, J. P. & Bertrand, P. O_2 reduction in PEM fuel cells: activity and active site structural information for catalysts obtained by the pyrolysis at high temperature of Fe precursors. *J. Phys. Chem. B* **104**, 11238–11247 (2000).
41. Pels, J. R., Kapteijn, F., Moulijn, J. A., Zhu, Q. & Thomas, K. M. Evolution of nitrogen functionalities in carbonaceous materials during pyrolysis. *Carbon* **33**, 1641–1653 (1995).
42. Li, H., Zhang, Z., Dou, M. & Wang, F. Towards high-performance electrocatalysts for oxygen reduction: inducing atomic-level reconstruction of Fe-N_x site for atomically dispersed Fe/N-doped hierarchically porous carbon. *Chem. - Eur. J.* **24**, 8848–8856 (2018).
43. Schulenburg, H. *et al.* Catalysts for the oxygen reduction from heat-treated iron(iii) tetramethoxyphenylporphyrin chloride: structure and stability of active sites. *J. Phys. Chem. B* **107**, 9034–9041 (2003).
44. Artyushkova, K. *et al.* Density functional theory calculations of XPS binding energy shift for nitrogen-containing graphene-like structures. *Chem. Commun.* **49**, 2539–2541 (2013).
45. Artyushkova, K., Walker, C., Patterson, W. & Atanassov, P. Hierarchically structured non-PGM oxygen reduction electrocatalyst based on microemulsion-templated silica and pyrolyzed iron and cyanamide precursors. *Electrocatalysis* **5**, 241–247 (2014).
46. Artyushkova, K., Serov, A., Rojas-Carbonell, S. & Atanassov, P. Chemistry of multitudinous active sites for oxygen reduction reaction in transition metal–nitrogen–carbon electrocatalysts. *J. Phys. Chem. C* **119**, 25917–25928 (2015).
47. Hossen, M. M., Artyushkova, K., Atanassov, P. & Serov, A. Synthesis and characterization of high performing Fe-N-C catalyst for oxygen reduction reaction (ORR) in alkaline exchange membrane fuel cells. *J. Power Sources* **375**, 214–221 (2018).
48. Chen, Y., Matanovic, I., Weiler, E., Atanassov, P. & Artyushkova, K. Mechanism of oxygen reduction reaction on transition metal–nitrogen–carbon catalysts: establishing the role of nitrogen-containing active sites. *ACS Appl. Energy Mater.* **1**, 5948–5953 (2018).
49. Strauss, S. H. *et al.* Comparison of the molecular and electronic structures of (2,3,7,8,12,13,17,18-octaethylporphyrinato)iron(ii) and (*trans*-7,8-dihydro-2,3,7,8,12,13,17,18-octaethylporphyrinato)iron(ii). *J. Am. Chem. Soc.* **107**, 4207–4215 (1985).
50. van Veen, J. A. R., van Baar, J. F. & Kroese, K. J. Effect of heat treatment on the performance of carbon-supported transition-metal chelates in the electrochemical reduction of oxygen. *J. Chem. Soc. Faraday Trans. 1* **77**, 2827–2843 (1981).
51. Collman, J. P., Hoard, J. L., Kim, N., Lang, G. & Reed, C. A. Synthesis, stereochemistry, and structure-related properties of α,β,γ,δ-tetraphenylporphinatoiron(II). *J. Am. Chem. Soc.* **97**, 2676–2681 (1975).
52. Polam, J. R. *et al.* Valence electron cloud asymmetry from two points of view: a correlation between Mössbauer quadrupole splittings and ^{57}Fe NMR chemical shifts of diamagnetic iron(ii) porphyrinates. *J. Am. Chem. Soc.* **118**, 5272–5276 (1996).
53. Dolphin, D., Sams, J. R., Tsin, T. B. & Wong, K. L. Synthesis and Moessbauer spectra of octaethylporphyrin ferrous complexes. *J. Am. Chem. Soc.* **98**, 6970–6975 (1976).
54. Dale, B. W., Williams, R. J. P., Edwards, P. R. & Johnson, C. E. *S* = 1 spin state of divalent iron. II. A Mössbauer- effect study of phthalocyanine iron (ii). *J. Chem. Phys.* **49**, 3445–3449 (1968).

55. Moss, T. H. & Robinson, A. B. Moessbauer experiments on iron(II) phthalocyanine. *Inorg. Chem.* **7**, 1692–1694 (1968).
56. Calderazzo, F. *et al.* Carbonyl derivatives of phthalocyaninatoiron(II), especially those containing group VI axial donor atoms. Crystal and molecular structure of carbonyl(*N,N*-dimethylformamide)phthalocyaninatoiron(II) and Mössbauer studies of some of the products. *J. Organomet. Chem.* **191**, 217–242 (1980).
57. Taube, R. New aspects of the chemistry of transition metal phthalocyanines. *Pure Appl. Chem.* **38**, 427–438 (1974).
58. Melendres, C. A. Moessbauer and Raman spectra of carbon-supported iron phthalocyanine. *J. Phys. Chem.* **84**, 1936–1939 (1980).
59. Filoti, G., Kuz'min, M. D. & Bartolomé, J. Mössbauer study of the hyperfine interactions and spin dynamics in α-iron(II) phthalocyanine. *Phys. Rev. B* **74**, 134420 (2006).
60. Koslowski, U. I., Abs-Wurmbach, I., Fiechter, S. & Bogdanoff, P. Nature of the catalytic centers of porphyrin-based electrocatalysts for the ORR: a correlation of kinetic current density with the site density of Fe−N_4 centers. *J. Phys. Chem. C* **112**, 15356–15366 (2008).
61. Chenitz, R. *et al.* A specific demetalation of Fe–N_4 catalytic sites in the micropores of NC_Ar + NH_3 is at the origin of the initial activity loss of the highly active Fe/N/C catalyst used for the reduction of oxygen in PEM fuel cells. *Energy Environ. Sci.* **11**, 365–382 (2018).
62. Wan, X. *et al.* Synthesis and active site identification of Fe−N−C single-atom catalysts for the oxygen reduction reaction. *ChemElectroChem* **6**, 304–315 (2019).
63. Workman, M. J., Serov, A., Tsui, L., Atanassov, P. & Artyushkova, K. Fe–N–C catalyst graphitic layer structure and fuel cell performance. *ACS Energy Lett.* **2**, 1489–1493 (2017).
64. Jiang, R. *et al.* Edge-site engineering of atomically dispersed Fe–N_4 by selective C–N bond cleavage for enhanced oxygen reduction reaction activities. *J. Am. Chem. Soc.* **140**, 11594–11598 (2018).
65. Liu, D. *et al. In situ* trapped high-density single metal atoms within graphene: iron-containing hybrids as representatives for efficient oxygen reduction. *Nano Res.* **11**, 2217–2228 (2018).
66. Chung, H. T. *et al.* Direct atomic-level insight into the active sites of a high-performance PGM-free ORR catalyst. *Science* **357**, 479–484 (2017).
67. Fei, H. *et al.* General synthesis and definitive structural identification of MN_4C_4 single-atom catalysts with tunable electrocatalytic activities. *Nat. Catal.* **1**, 63–72 (2018).
68. Savéant, J.-M. Molecular catalysis of electrochemical reactions. Mechanistic aspects. *Chem. Rev.* **108**, 2348–2378 (2008).
69. Costentin, C. & Savéant, J.-M. Homogeneous molecular catalysis of electrochemical reactions: catalyst benchmarking and optimization strategies. *J. Am. Chem. Soc.* **139**, 8245–8250 (2017).
70. Mittra, K., Chatterjee, S., Samanta, S. & Dey, A. Selective $4e^-/4H^+$ O_2 reduction by an iron(tetraferrocenyl)porphyrin complex: from proton transfer followed by electron transfer in organic solvent to proton coupled electron transfer in aqueous medium. *Inorg. Chem.* **52**, 14317–14325 (2013).
71. Bhunia, S. *et al.* Rational design of mononuclear iron porphyrins for facile and selective $4e^-/4H^+$ O_2 reduction: activation of O–O bond by 2nd sphere hydrogen bonding. *J. Am. Chem. Soc.* **140**, 9444–9457 (2018).
72. Pegis, M. L. *et al.* Homogenous electrocatalytic oxygen reduction rates correlate with reaction overpotential in acidic organic solutions. *ACS Cent. Sci.* **2**, 850–856 (2016).
73. Pegis, M. L., Wise, C. F., Koronkiewicz, B. & Mayer, J. M. Identifying and breaking scaling relations in molecular catalysis of electrochemical reactions. *J. Am. Chem. Soc.* **139**, 11000–11003 (2017).
74. Pegis, M. L., Wise, C. F., Martin, D. J. & Mayer, J. M. Oxygen reduction by homogeneous molecular catalysts and electrocatalysts. *Chem. Rev.* **118**, 2340–2391 (2018).
75. Baran, J. D., Grönbeck, H. & Hellman, A. Analysis of porphyrines as catalysts for electrochemical reduction of O_2 and oxidation of H_2O. *J. Am. Chem. Soc.* **136**, 1320–1326 (2014).
76. Lovecchio, F. V., Gore, E. S. & Busch, D. H. Oxidation and reduction behavior of macrocyclic complexes of nickel. Electrochemical and electron spin resonance studies. *J. Am. Chem. Soc.* **96**, 3109–3118 (1974).
77. van Baar, J. F., van Veen, J. A. R., van der Eijk, J. M., Peters, Th. J. & de Wit, N. Electrochemical oxidation of carbon monoxide with carbon-supported group VIII metal chelates: mechanistic aspects. *Electrochim. Acta* **27**, 1315–1319 (1982).
78. Ogawa, S., Yamaguchi, T. & Gotoh, N. Synthesis of a novel macrocyclic compound and of its copper complex. *J. Chem. Soc. Chem. Commun.* 577–578 (1972).

79. Ogawa, S., Yamaguchi, T. & Gotoh, N. Preparation of a conjugated tautomer of 1,14:7,8-diethenotetrapyrido-[2,1,6-*de*:2′,1′,6′-*gh*:2″,1″,6″-*kl*:2‴,1‴,6‴*na*][1,3,5,8,10,12]hexa-azacyclotetradecine and its metal derivatives. *J. Chem. Soc., Perkin Trans. 1,* 976–978 (1974).
80. Ogawa, S. Preparation of macrocyclic compounds by thermal dimerization of 1,10-phenanthroline derivatives. *J. Chem. Soc., Perkin Trans. 1,* 214–216 (1977).
81. Endres, H. & Hunziker, M. Crystal and molecular structure of a hexaazamacrocycle. *J. Cryst. Mol. Struct.* **9**, 77–85 (1979).
82. Wang, W.-J., Liu, H.-Y., Chuang, K.-S. & Luo, C.-F. Copper 1,14:7,8-diethenotetrapyrido-[2,1,6-*de*:2',1',6'-*gh*:2'',1'',6'''-*na*][1,3,5,8,10,12]hexaazacyclotetradecine trifluoroacetate. *Molecules* **5**, M133 (2000).
83. Wang, W.-J., Chuang, K.-S., Luo, C.-F. & Liu, H.-Y. An efficient one-pot route to an aza-bridged bis-phenanthroline macrocyclic compound. *Tetrahedron Lett.* **41**, 8565–8568 (2000).
84. Cheng, C.-C., Kuo, Y.-N., Chuang, K.-S., Luo, C.-F. & Wang, W. J. A new Co^{II} complex as a bulge-specific probe for DNA. *Angew. Chem. Int. Ed.* **38**, 1255–1257 (1999).
85. Costamagna, J. *et al.* Precursors of aza-macrocycles: characterization of substituted phenanthrolines and related bases. Crystal and molecular structure of dichloro-d i-*n*-butyl(2,2',6,6'-bipyrimidine)tin(iv). *Pure Appl. Chem.* **65**, 1521–1526 (1993).
86. Vargas, J., Ferraudi, G., Canale, J. & Costamagna, J. Reduction of hexaazacyclophane complexes of Co(II) and Cu(II) by $^{\bullet}CH_2OH$ and e_{sol}^{-}; A pulse radiolysis study. *Inorganica Chim. Acta* **226**, 151–157 (1994).
87. Isaacs, M. *et al.* Electrocatalytic reduction of CO_2 by aza-macrocyclic complexes of Ni(II), Co(II), and Cu(II). Theoretical contribution to probable mechanisms. *Inorganica Chim. Acta* **339**, 224–232 (2002).
88. Canales, J., Ramirez, J., Estiu, G. & Costamagna, J. Bis-bipyridine hexa-aza-macrocycle complexes of zinc(II) and nickel(II) and the catalytic reduction of carbon dioxide. *Polyhedron* **19**, 2373–2381 (2000).
89. Kramm, U. I. *et al.* On an easy way to prepare metal–nitrogen doped carbon with exclusive presence of MeN_4-type sites active for the ORR. *J. Am. Chem. Soc.* **138**, 635–640 (2016).
90. Mineva, T. *et al.* Understanding active sites in pyrolyzed Fe-N-C catalysts for fuel cell cathodes by bridging density functional theory calculations and ^{57}Fe Mössbauer spectroscopy. *ACS Catal.* **9**, 9359–9371 (2019).
91. White, A. D. Iron(III) Chloride-Dimethylformamide. in *Encyclopedia of Reagents for Organic Synthesis* (2001). doi:10.1002/047084289X.ri058.
92. Sustmann, R. *et al.* Fe^{III} complexes of 1,4,8,11-tetraaza[14]annulenes as catalase mimics. *Inorg. Chem.* **46**, 11416–11430 (2007).
93. Vaishnava, P. P. & Montano, P. A. *In situ* Mössbauer spectroscopic study of iron III chloride intercalated in graphite under reaction conditions. *J. Phys. Chem. Solids* **43**, 809–815 (1982).
94. Schlögl, R. & Jones, W. On the structure and properties of iron halide–graphite intercalates: a comparison of the reactivity of free and graphite-intercalated iron(III) chloride. *J. Chem. Soc. Dalton Trans.* 1283–1292 (1984).
95. Kastner, M. E., Scheidt, W. R., Mashiko, T. & Reed, C. A. Molecular structure of diaquo-α,β,ɣ,δ-tetraphenylporphinatoiron(III) perchlorate and perchlorato-α,β,ɣ,δ-tetraphenylporphinatoiron(III). Two new structural types for iron(III) porphyrins. *J. Am. Chem. Soc.* **100**, 666–667 (1978).
96. Reed, C. A. *et al.* The missing heme spin state and a model for cytochrome c'. The mixed $S = 3/2, 5/2$ intermediate spin ferric porphyrin: perchlorato(meso-tetraphenylporphinato)iron(III). *J. Am. Chem. Soc.* **101**, 2948–2958 (1979).
97. Sakai, T. *et al.* Electronic structures of five-coordinate iron(III) porphyrin complexes with highly ruffled porphyrin ring. *Inorg. Chem.* **43**, 5034–5043 (2004).
98. Schünemann, V. *et al.* The 5/2,3/2 spin admixture in the chloroiron(III) derivative of the sterically crowded 2,3,7,8,12,13,17,18-octaethyl-5,10,15,20-tetraphenylporphyrin. *Angew. Chem. Int. Ed.* **38**, 3181–3183 (1999).
99. Sahoo, D. & Rath, S. P. Controlled generation of highly saddled (porphyrinato)iron(III) iodide, tri-iodide and one-electron oxidized complexes. *Chem. Commun.* **51**, 16790–16793 (2015).
100. Dolphin, D. H., Sams, J. R. & Tsin, T. Bik. Intermediate-spin ($S = 3/2$) porphyrinatoiron(III) complexes. *Inorg. Chem.* **16**, 711–713 (1977).
101. Sams, J. R. & Tsin, T. B. Mössbauer Spectroscopy of Iron Porphyrins. in *The Porphyrins* 425–478 (Elsevier, 1979). doi:10.1016/B978-0-12-220104-2.50016-8.
102. Ling, Y. & Zhang, Y. Mössbauer, NMR, geometric, and electronic properties in $S = {}^3/_2$ iron porphyrins. *J. Am. Chem. Soc.* **131**, 6386–6388 (2009).
103. Ohgo, Y. *et al.* Molecular structures of five-coordinated halide ligated iron(III) porphyrin, porphycene, and corrphycene complexes. *Inorg. Chem.* **41**, 4627–4629 (2002).

104. Fitzgerald, J. P., Haggerty, B. S., Rheingold, A. L., May, L. & Brewer, G. A. Iron octaethyltetraazaporphyrins: synthesis, characterization, coordination chemistry, and comparisons to related iron porphyrins and phthalocyanines. *Inorg. Chem.* **31**, 2006–2013 (1992).
105. Keutel, H. *et al.* Structural, magnetic, and electronic properties of a pentacoordinated intermediate-spin ($S = {}^3/_2$) iron(III) complex with a macrocyclic $[N_4]^{2-}$ ligand. *Inorg. Chem.* **38**, 2320–2327 (1999).
106. Kojima, T. *et al.* Intermediate-spin iron(III) complexes having a redox-noninnocent macrocyclic tetraamido ligand. *Inorg. Chem.* **57**, 9683–9695 (2018).
107. Cheng, B. *et al.* An unusual near-eclipsed porphyrin ring orientation in two crystalline forms of (μ-oxo)bis[(octaethylporphinato)iron(III)]. Structural and molecular mechanics studies. *Inorg. Chem.* **34**, 102–110 (1995).
108. Sinha, S., Aaron, M. S., Blagojevic, J. & Warren, J. J. Electrocatalytic dioxygen reduction by carbon electrodes noncovalently modified with iron porphyrin complexes: enhancements from a single proton relay. *Chem. - Eur. J.* **21**, 18072–18075 (2015).
109. Götz, R., Ly, H. K., Wrzolek, P., Schwalbe, M. & Weidinger, I. M. Surface enhanced resonance Raman spectroscopy of iron Hangman complexes on electrodes during electrocatalytic oxygen reduction: advantages and problems of common drycast methods. *Dalton Trans.* **46**, 13220–13228 (2017).
110. Dolphin, D. H., Sams, J. R., Tsin, T. B. & Wong, K. L. Moessbauer-Zeeman spectra of some octaethylporphyrinato- and tetraphenylporphinatoiron(III) complexes. *J. Am. Chem. Soc.* **100**, 1711–1718 (1978).
111. Zhang, Z., Sun, J., Wang, F. & Dai, L. Efficient oxygen reduction reaction (ORR) catalysts based on single iron atoms dispersed on a hierarchically structured porous carbon framework. *Angew. Chem. Int. Ed.* **57**, 9038–9043 (2018).
112. Lin, L., Zhu, Q. & Xu, A.-W. Noble-metal-free Fe–N/C catalyst for highly efficient oxygen reduction reaction under both alkaline and acidic conditions. *J. Am. Chem. Soc.* **136**, 11027–11033 (2014).
113. Lavallee, D. K., Brace, J. & Winograd, N. X-ray photoelectron spectra of N-methyltetraphenylporphyrins: evidence for a correlation of binding energies with metal-nitrogen bond distances. *Inorg. Chem.* **18**, 1776–1780 (1979).
114. Muralidharan, S. & Hayes, R. G. Intense satellites in the N 1s X-ray photoelectron spectra of certain metalloporphyrins. *J. Am. Chem. Soc.* **102**, 5106–5107 (1980).
115. Nemykin, V. N. *et al.* Metal-free and transition-metal tetraferrocenylporphyrins part 1: synthesis, characterization, electronic structure, and conformational flexibility of neutral compounds. *Dalton Trans.* 4233–4246 (2008).
116. Jia, H., Sun, Z., Jiang, D., Yang, S. & Du, P. An iron porphyrin-based conjugated network wrapped around carbon nanotubes as a noble-metal-free electrocatalyst for efficient oxygen reduction reaction. *Inorg. Chem. Front.* **3**, 821–827 (2016).
117. Ouedraogo, G. V., Benlian, D. & Porte, L. X- ray photoelectron spectroscopy of phthalocyanine compounds. *J. Chem. Phys.* **73**, 642–647 (1980).
118. Åhlund, J. *et al.* The electronic structure of iron phthalocyanine probed by photoelectron and x-ray absorption spectroscopies and density functional theory calculations. *J. Chem. Phys.* **125**, 034709 (2006).
119. Grosvenor, A. P., Kobe, B. A., Biesinger, M. C. & McIntyre, N. S. Investigation of multiplet splitting of Fe 2p XPS spectra and bonding in iron compounds. *Surf. Interface Anal.* **36**, 1564–1574 (2004).
120. Sa, Y. J. *et al.* A general approach to preferential formation of active Fe–N_x sites in Fe–N/C electrocatalysts for efficient oxygen reduction reaction. *J. Am. Chem. Soc.* **138**, 15046–15056 (2016).
121. Colomban, C. *et al.* Synthesis and characterization of μ-nitrido, μ-carbido and μ-oxo dimers of iron octapropylporphyrazine. *Dalton Trans.* **44**, 2240–2251 (2015).
122. Lee, H. M., Olmstead, M. M., Gross, G. G. & Balch, A. L. Cocrystallization of binuclear iron(III) porphyrins with C_{60}: bending of μ-O{Fe^{III}(octaethylporphyrin)} and the first structure of the iron(III) octaethyloxophlorin dimer. *Cryst. Growth Des.* **3**, 691–697 (2003).
123. Westre, T. E. *et al.* A multiplet analysis of Fe K-edge 1s → 3d pre-edge features of iron complexes. *J. Am. Chem. Soc.* **119**, 6297–6314 (1997).
124. Salimi, A., MamKhezri, H., Hallaj, R. & Zandi, S. Modification of glassy carbon electrode with multi-walled carbon nanotubes and iron(III)-porphyrin film: application to chlorate, bromate and iodate detection. *Electrochim. Acta* **52**, 6097–6105 (2007).
125. Zhang, L., Song, C., Zhang, J., Wang, H. & Wilkinson, D. P. Temperature and pH dependence of oxygen reduction catalyzed by iron fluoroporphyrin adsorbed on a graphite electrode. *J. Electrochem. Soc.* **152**, A2421 (2005).

126. Li, J. *et al.* Structural and mechanistic basis for the high activity of Fe–N–C catalysts toward oxygen reduction. *Energy Environ. Sci.* **9**, 2418–2432 (2016).
127. Zúñiga, C. *et al.* Elucidating the mechanism of the oxygen reduction reaction for pyrolyzed Fe-N-C catalysts in basic media. *Electrochem. Commun.* **102**, 78–82 (2019).
128. Jackson, M. N., Pegis, M. L. & Surendranath, Y. Graphite-conjugated acids reveal a molecular framework for proton-coupled electron transfer at electrode surfaces. *ACS Cent. Sci.* **5**, 831–841 (2019).
129. Jackson, M. N. *et al.* Strong electronic coupling of molecular sites to graphitic electrodes via pyrazine conjugation. *J. Am. Chem. Soc.* **140**, 1004–1010 (2018).
130. Kaminsky, C. J., Wright, J. & Surendranath, Y. Graphite-conjugation enhances porphyrin electrocatalysis. *ACS Catal.* **9**, 3667–3671 (2019).
131. Masa, J., Zhao, A., Xia, W., Muhler, M. & Schuhmann, W. Metal-free catalysts for oxygen reduction in alkaline electrolytes: influence of the presence of Co, Fe, Mn and Ni inclusions. *Electrochim. Acta* **128**, 271–278 (2014).
132. Artyushkova, K., Matanovic, I., Halevi, B. & Atanassov, P. Oxygen binding to active sites of Fe–N–C ORR electrocatalysts observed by ambient-pressure XPS. *J. Phys. Chem. C* **121**, 2836–2843 (2017).
133. Sarapuu, A., Kibena-Põldsepp, E., Borghei, M. & Tammeveski, K. Electrocatalysis of oxygen reduction on heteroatom-doped nanocarbons and transition metal–nitrogen–carbon catalysts for alkaline membrane fuel cells. *J. Mater. Chem. A* **6**, 776–804 (2018).
134. Sun, Y. *et al.* Efficient electrochemical hydrogen peroxide production from molecular oxygen on nitrogen-doped mesoporous carbon catalysts. *ACS Catal.* **8**, 2844–2856 (2018).
135. van Veen, J. A. R. *et al.* Oxygen reduction on transition-metal porphyrins in acid electrolyte I. Activity. *Berichte Bunsenges. Für Phys. Chem.* **85**, 693–700 (1981).
136. van Veen, J. A. R. & Colijn, H. A. Oxygen reduction on transition-metal porphyrins in acid electrolyte II. Stability. *Berichte Bunsenges. Für Phys. Chem.* **85**, 700–704 (1981).
137. Baranton, S., Coutanceau, C., Roux, C., Hahn, F. & Léger, J.-M. Oxygen reduction reaction in acid medium at iron phthalocyanine dispersed on high surface area carbon substrate: tolerance to methanol, stability and kinetics. *J. Electroanal. Chem.* **577**, 223–234 (2005).
138. Choi, C. H. *et al.* The Achilles' heel of iron-based catalysts during oxygen reduction in an acidic medium. *Energy Environ. Sci.* **11**, 3176–3182 (2018).
139. Wang, W.-J., Sengul, A., Luo, C.-F., Kao, H.-C. & Cheng, Y.-H. Facile one-step synthesis of a thia-bridged bis-1,10-phenanthroline macrocycle. *Tetrahedron Lett.* **44**, 7099–7101 (2003).
140. Krapcho, A. P., Sparapani, S., Leenstra, A. & Seitz, J. D. Displacement reactions of 2-chloro- and 2,9-dichloro-1,10-phenanthroline: synthesis of a sulfur-bridged bis-1,10-phenanthroline macrocycle and a 2,2′-amino-substituted-bis-1,10-phenanthroline. *Tetrahedron Lett.* **50**, 3195–3197 (2009).
141. Costentin, C., Drouet, S., Robert, M. & Savéant, J.-M. A local proton source enhances CO_2 electroreduction to CO by a molecular Fe catalyst. *Science* **338**, 90–94 (2012).
142. Azcarate, I., Costentin, C., Robert, M. & Savéant, J.-M. Through-space charge interaction substituent effects in molecular catalysis leading to the design of the most efficient catalyst of CO_2-to-CO electrochemical conversion. *J. Am. Chem. Soc.* **138**, 16639–16644 (2016).
143. Costentin, C. & Savéant, J.-M. Towards an intelligent design of molecular electrocatalysts. *Nat. Rev. Chem.* **1**, 0087 (2017).
144. Yeh, C.-Y., Chang, C. J. & Nocera, D. G. "Hangman" porphyrins for the assembly of a model heme water channel. *J. Am. Chem. Soc.* **123**, 1513–1514 (2001).
145. Chang, C. J., Loh, Z.-H., Shi, C., Anson, F. C. & Nocera, D. G. Targeted proton delivery in the catalyzed reduction of oxygen to water by bimetallic pacman porphyrins. *J. Am. Chem. Soc.* **126**, 10013–10020 (2004).
146. McGuire Jr., R. *et al.* Oxygen reduction reactivity of cobalt(II) hangman porphyrins. *Chem. Sci.* **1**, 411–414 (2010).
147. Roubelakis, M. M., Bediako, D. K., Dogutan, D. K. & Nocera, D. G. Proton-coupled electron transfer kinetics for the hydrogen evolution reaction of hangman porphyrins. *Energy Environ. Sci.* **5**, 7737–7740 (2012).
148. Bediako, D. K. *et al.* Role of pendant proton relays and proton-coupled electron transfer on the hydrogen evolution reaction by nickel hangman porphyrins. *Proc. Natl. Acad. Sci.* **111**, 15001–15006 (2014).
149. Kirchon, A., Feng, L., Drake, H. F., Joseph, E. A. & Zhou, H.-C. From fundamentals to applications: a toolbox for robust and multifunctional MOF materials. *Chem. Soc. Rev.* **47**, 8611–8638 (2018).
150. Rogge, S. M. J. *et al.* Metal–organic and covalent organic frameworks as single-site catalysts. *Chem. Soc. Rev.* **46**, 3134–3184 (2017).